

Size-Dependent Adsorption and Adhesion Energetics of Ag Nanoparticles on Graphene Films on Ni(111) by Calorimetry

John R. Rumpitz¹, Zhongtian Mao^{2,a}, and Charles T. Campbell^{1,2,*}

¹Department of Chemical Engineering, and ²Department of Chemistry
University of Washington
Seattle, Washington 98105-1700, USA

^a Current address:

Chemistry Division, Brookhaven National Laboratory, Upton, NY 11973, USA

Abstract

Interest in the use of carbon supports for late transition metal nanoparticle catalysts has expanded rapidly due to the increasing importance of electrocatalysts for clean energy and environmental technologies and the use and storage of renewable electricity. Compared to oxide supports, almost nothing is known about the effect of metal nanoparticle size on the energies of the metal atoms within carbon-supported nanoparticles, yet these energies are crucial for understanding their surface reactivity and sintering kinetics. Here, the growth morphology and adsorption energetics of vapor-deposited Ag onto clean graphene / Ni(111) surfaces have been studied using a combination of single crystal adsorption calorimetry (SCAC) and He⁺ low-energy ion scattering (LEIS). The differential heat of Ag adsorption is 207 kJ/mol for making ~30-atom Ag particles on graphene terraces at 100 K, and 16 kJ/mol higher for making ~9-atom Ag clusters at defect sites at the same temperature. The heat of adsorption increases rapidly with Ag coverage as 3D Ag nanoparticles nucleate and grow in size, asymptotically reaching within 5 kJ/mol of the bulk Ag sublimation enthalpy (285 kJ/mol) by 2 ML. The heats of adsorption and Ag nanoparticle densities from LEIS ($\sim 10^{16}/\text{m}^2$) were combined to provide the Ag / graphene adhesion energy ($E_{adh} = 1.8 \text{ J/m}^2$ in the large-particle limit) and the Ag chemical potential (μ) versus effective particle diameter (D). The Ag chemical potential was well fitted by: $\mu(D) = (3\gamma_{v/M} - E_{adh})(1 + (1.5 \text{ nm})/D)(2V_m/D)$, where $\gamma_{v/M}$ is the surface energy of bulk Ag, and V_m is its molar volume. The same equation is known to fit similar data for late transition metals on clean surfaces of metal oxide single crystals. The adhesion energy of Ag measured here on graphene falls within the wide range measured for Ag on those oxide surfaces, and is almost as large as on that oxide which binds Ag particles most strongly, namely CeO₂(111), which is well known to be very effective at resisting catalyst deactivation by metal sintering. These results imply that carbon supports will be effective at resisting sintering, and that Ag particles smaller than 6 nm on graphene will bind small adsorbed reaction intermediates more weakly than supports with weaker adhesion to Ag, like MgO(100).

Keywords: carbon supports, graphene, nanoparticle size effects, support effects, metal/carbon interface, adhesion energy, chemical potential, sintering rates.

* Corresponding author: charliec@uw.edu

1. Introduction

Late transition metal nanoparticles supported on high surface area support materials are important heterogeneous catalysts and electrocatalysts for energy, environmental, and chemical technologies. It is well known that the performance of these metal nanoparticle catalysts are influenced strongly by the choices of metal and support material, and by the metal nanoparticle size and structure.¹⁻⁸ These performance-based properties include the catalytic activity, selectivity, and long-term thermal stability of the metal / support system. As such, a better fundamental understanding of these structure-performance relationships will help to design new catalyst materials with more desirable properties for technological purposes. Our group has shown that the chemical potential of metal atoms in supported nanoparticles provides a convenient descriptor of their performance as heterogeneous catalysts that captures many of the effects of particle size, support and even alloying.⁹⁻¹¹

Using microcalorimetric measurements of the differential heats of adsorption of metal vapor as it adds to pre-deposited metal nanoparticles on the surfaces of single-crystalline oxide supports, our group has determined this metal-atom chemical potential as a function of particle diameter for monometallic nanoparticles on different oxide supports.^{9,10} It was found from these measurements that this chemical potential has a predictable dependence upon the particle size and the adhesion energy at the particle / support interface.^{9,10} Furthermore, this adhesion energy was measured for many combinations of late transition metals and oxide supports and found to follow some predictable trends.¹⁰ However, all those results are for oxide support materials (like CeO₂(111), MgO(100), etc.). Essentially nothing is known about the chemical potential versus nanoparticle size for metal on carbon-based supports. Here, we report the first experimental measurements of the metal chemical potential versus particle size for nanoparticles of any metal element on any carbon support material, specifically for Ag nanoparticles supported on single-layer graphene(0001) on Ni(111). We also report the metal / support adhesion energy for that Ag / graphene interface. The only other experimental metal / graphene adhesion energy of which we are aware is for Ni on graphene / Ni(111), based on particle shape measurements with scanning tunneling microscopy (STM).¹² Both the Ag chemical potential and Ag / graphene adhesion energy are determined here from heats of Ag vapor adsorption versus Ag coverage on clean graphene as Ag nanoparticles nucleate and grow in size on the surface, measured using single crystal adsorption calorimetry (SCAC). To the best of our knowledge, this is also the first SCAC measurement of the adsorption energetics of any metal vapor on any carbon-based support system, and *the first measurements of chemical potential versus size for nanoparticles of any metal on any carbon support*. The results show that such a carbon support binds Ag nanoparticles nearly as strongly as the previously-measured oxide which binds Ag nanoparticles most strongly, CeO₂(111), and that the Ag chemical potential for a given nanoparticle size below 6 nm is only slightly higher for Ag on this carbon support than for Ag on CeO₂(111), but much lower than for Ag on a weak-binding support like MgO. Given reported correlations between metal chemical potential and catalyst performance (i.e., sinter resistance and bonding strength to small adsorbates),^{9-11,13-16} this further suggests that such carbon supports will be almost as effective for resisting catalyst deactivation by sintering as CeO₂(111), and that small adsorbed reaction intermediates will bind to Ag nanoparticles rather weakly.

The use of carbon as a support material has become increasingly common,^{17–22} in part because carbon is conductive and can serve as an electrode material for electrocatalysis, and the increasing importance of electrocatalysis for clean-energy storage. Whether it is in the form of activated carbon, carbon black, modified graphite, carbon nanofibers or carbon nanotubes, the dominant building block in a carbon support's structure is the graphite unit cell.²¹ There are extensive modifications that can be made to C(0001) to change its surface properties including creating sputter-induced defects,^{23–25} partial oxidation of the surface,²¹ and chemical doping.^{26,27} The many applications of the C(0001) surface as well as its extensive modifications make it an attractive material surface for research.

Silver nanoparticles supported on carbon form the basis for one of the best electrocatalysts for CO₂ reduction to CO,¹⁸ a very important reaction for clean energy. Silver nanoparticles on oxide supports are also commonly employed as selective oxidation catalysts, for example in methanol partial oxidation and ethylene epoxidation.^{28–32} It is thus unsurprising that many groups are beginning to investigate silver on carbon-based supports for electrocatalytic oxidation reactions as well.^{33–35} In addition, due to unique optoelectronic properties, silver nanoparticles have been shown to have increased reactivity due to surface plasmon resonance and find applications in surface enhanced Raman spectroscopy (SERS).^{36–39}

There have been many previous studies of the adsorption of gaseous Ag monomers and small clusters on graphite and graphene surfaces using both experimental methods^{24,38–46} and theoretical methods^{24,46–52} (typically density functional theory). While the exact results of these studies can vary tremendously with the methods used, there is some consensus that a weak interaction between Ag metal and the graphite support leads to the clustering of Ag monomers to form 3D particles.^{24,40,41,47,51} Microscopy images show that these particles grow preferentially at the step edges when grown on graphite at room temperature and above.^{40,41}

In this paper, we study the bonding energetics of Ag atoms in Ag nanoparticles grown by Ag vapor deposition on a single layer of graphene supported on Ni(111) using SCAC. The single-layer graphene films studied here were grown on clean Ni(111) using a method described in the literature.^{12,53,54} This produces a single atomic layer of C(0001) with an in-plane lattice constant within 1.5% of that in bulk graphite(0001), in registry with the underlying Ni(111) surface, with two carbon atoms per Ni atom.^{25,53–55} Due to the strong in-plane bonding and weak bonding between (0001) layers in graphite, the surface binding of Ag to this single layer of graphene(0001) is expected to approximate that for thicker graphite(0001) surfaces, although the interaction with the underlying Ni(111) is likely to have some effect. The particle density and growing Ag nanoparticle size is measured using low-energy ion scattering (LEIS). Using the coverage dependent heats of adsorption of Ag vapor along with the particle size from LEIS, we determine the Ag chemical potential versus particle size and the Ag(solid) / C(0001) adhesion energy. The results presented here help to explain the morphology and chemical bonding of metal nanoparticles supported on carbon-based materials.

2. Experimental Methods

A full description of the single crystal adsorption calorimetry (SCAC) apparatus and detailed experimental procedures is presented elsewhere.⁵⁶ Briefly, the calorimetry experiments were done in an ultrahigh vacuum (UHV) chamber with a base pressure $< 2 \times 10^{-10}$ torr. This chamber is also equipped with X-ray photoelectron spectroscopy (XPS), Auger electron spectroscopy (AES), He⁺ low-energy ion scattering (LEIS), low-energy electron diffraction (LEED), quadrupole mass spectrometry (QMS), and two quartz crystal microbalances (QCMs). Surface spectroscopy measurements were obtained with a PHI 10-360 precision energy analyzer with a PHI 72-250 position sensitive detector.

The Ag metal beam is generated by evaporating Ag pellets in an e-beam evaporator. The Ag vapor is collimated through a series of apertures to give an average beam diameter of 4.26 mm. The beam is then pulsed with a chopper with a pulse duration of 100 ms and a period of 2 s. The Ag flux is monitored with two QCMs; one on-axis QCM to measure the flux at the sample position (possible only just before and just after calorimetry), and another off-axis QCM to continuously monitor the flux during the experiment. The flux varies with time (typically dropping by $\sim 15\%$ during a run), so the continuously-measured off-axis flux was scaled at all times in a method described previously to provide the flux at all times at the sample position.⁵⁶

The heat released is measured using a pyroelectric polyvinylidene fluoride (PVDF) ribbon in physical and thermal contact with the 1 μm thick Ni(111) single crystal sample. The PVDF ribbon is calibrated for each experiment using a HeNe laser with known energy. The total heat detected with the PVDF ribbon is a combination of the heat of adsorption as well as the thermal radiation from the hot metal source. The signal from thermal radiation was measured by placing a barium fluoride (BaF₂) window in front of the sample to block Ag atoms from reaching the sample but allowing a known fraction of thermal radiation to transmit through the window ($> 90\%$, measured with and without the window in the path). The resulting signal from thermal radiation was then subtracted from the total heat signal. The measured heat was further corrected to account for the difference in internal (translational) energy between the directed flux of gas-phase Ag atoms coming from the high temperature electron beam evaporator (~ 1380 K)⁵⁷ and a collection of the same gas atoms in a Boltzmann distribution at the surface temperature (300 K or 100 K). The resulting heat is thereby equal to the negative of the standard enthalpy of Ag adsorption at the sample temperature.

The sticking probability of each pulse is measured simultaneously with the adsorption heats using a modified King and Well's method described previously.^{56,58} The number of Ag atoms that stick to the sample surface in each pulse is then equal to the flux times the pulse duration and the sticking probability. The differential heat of adsorption per mole of adsorbed Ag as a function of the cumulative Ag coverage can then be calculated from the measured heats, fluxes, and sticking probabilities. The Ag coverages reported here are given in units of ML, with 1 ML defined as 1.87×10^{19} atoms/m², which is the areal density of Ni atoms on the Ni(111) surface as well as exactly $\frac{1}{2}$ the areal density of C atoms on the graphene surface which grows in registry with the Ni(111) substrate.^{25,55}

3. Results and Discussion

3.1 Graphene Growth and Characterization

Graphene films were grown on a clean 1 μm thick Ni(111) single crystal using a direct growth method described in the literature.^{12,53,54} Before growth, the Ni(111) sample was cleaned by cycles of flashing the sample at 800 °C followed by 1.0 kV Ar⁺ ion sputtering until the presence of the C-1s carbon peak could not be detected by XPS. The clean Ni(111) sample was then annealed in vacuum at 600-650 °C for 5 mins before exposing the sample to 10⁻⁶ torr ethylene for 30 mins while holding the sample at 600-650 °C. After growth, the presence of graphene was confirmed by AES. Previous work has shown that the C-KVV AES line has a distinctive shape for graphitic and carbidic carbon, which allowed an easy determination of the surface phase.^{12,59,60} In line with previous work, we found that samples grown at temperatures below 500 °C showed the presence of nickel carbide while samples grown between 600-650 °C consistently showed the line-shape characteristic of graphene.¹² The quality of the graphene films was further confirmed by He⁺ LEIS. For a complete graphene film, the nickel LEIS signal attenuates > 95% (relative to clean Ni), while the nickel LEIS signal is still apparent for an incomplete film.

3.2 Ag Sticking Probability on Graphene / Ni(111)

The sticking probability of Ag atoms to graphene / Ni(111) was monitored during calorimetry experiments by measuring the transient QMS signal of Ag atoms during each deposited pulse. This signal was then normalized to a zero-sticking signal of Ag atoms pulsed onto a hot W flag where no permanent sticking occurs, as described by our group previously.⁶¹ The fraction of atoms that stick times the Ag vapor flux was then used to scale the absorbed heat per pulse and the accumulated Ag coverage during all experiments.

The sticking probabilities versus coverage at 300 K and 100 K are shown in Figure 1. The Ag coverages reported here are given in units of ML, with 1 ML defined as 1.87×10^{19} atoms/m², which is the areal density of Ni atoms on the Ni(111) surface as well as exactly ½ the areal density of C atoms on the graphene surface which grows in registry with the Ni(111) substrate.^{25,55} At 300 K, the sticking probability starts low at 75% and increases slowly to a value of 86% by 4 ML. At 100K, the sticking probability starts much higher at an initial value of 87% and gradually rises to a value slightly greater than 98% at the highest coverages measured. The decrease in sticking probabilities with increasing surface temperature is commonly reported for metal adsorption, where it has been attributed primarily to the increased desorption rate of diffusing metal adatoms as the temperature is raised.^{62,63} Since the ratio of desorption rate to diffusion rate is much greater at 300 K in comparison to 100 K, diffusing Ag adatoms are much more likely to desorb at this higher temperature before they find other Ag adatoms or Ag clusters to which they can bond.

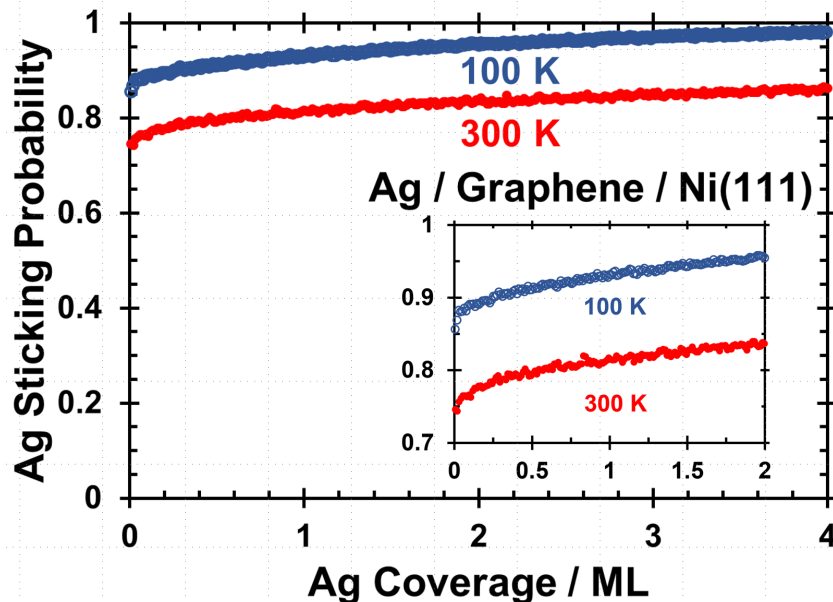


Figure 1: Sticking probability of Ag gas atoms onto graphene / Ni(111) as a function of Ag coverage at 300 K (red, filled points) and 100 K (blue, open points). The absolute coverage of 1 ML here is defined as 1.87×10^{19} atoms/m².

3.3 Ag Growth Morphology on Graphene / Ni(111)

The Ag growth morphology on graphene / Ni(111) at 300 K and 100 K was determined using He⁺ LEIS measurements. Gaseous Ag was deposited onto the graphene / Ni(111) substrate in discrete amounts and the Ag LEIS signal was measured after each dose. In contrast to previous systems studied by our group with LEIS, the substrate's LEIS signal (for the element C in this present study) could not be measured due to near unity ion neutralization probability for He⁺ ions scattering off of graphitic carbon species.⁶⁴⁻⁶⁶ The integrated Ag LEIS signal was normalized to the signal from a thick Ag overlayer (>10 nm), which served as the Ag reference signal of complete coverage of the surface by Ag. This normalized Ag LEIS signal then gives the fraction of the surface covered and shadowed by Ag particles.

The resulting integrated Ag LEIS signal versus Ag coverage is shown in Figure 2 and is compared with two growth models. The layer-by-layer growth model (shown as a straight black dashed line) corresponds to the signal that would be observed if Ag grew in a layer-by-layer fashion. As can be seen in Figure 2, this model does not fit the data well. The solid lines correspond to a hemispherical cap growth model first described by Diebold et al. in which all particles are assumed to have the same hemispherical shape and same particle size at a given coverage and temperature.^{67,68} Furthermore, the particles are assumed to have a constant number density at all coverages in agreement with classical nucleation theory in which a saturation number density is reached after a very small initial nucleation stage on the order of a few percent of a ML.^{1,69} This hemispherical cap model is applied only up to coverages at which <33% of the surface is covered by particles because at higher coverages the particles will begin to overlap and

the model assumptions break down. As described previously,⁶⁸ the hemispherical cap model predicts the normalized Ag LEIS intensity increases with the particle density and coverage as expressed in the following equation:

$$\frac{I(\theta)}{I(\theta = \infty)} = \pi f_{shadowing} \left(\frac{3 \theta n_{ML} M_{Ag}}{2\pi N_A \rho_{Ag}} \right)^{2/3} n^{1/3} , \quad (1)$$

where θ is the coverage, $[I(\theta)/I(\theta = \infty)]$ is the normalized Ag LEIS signal, n_{ML} is the monolayer definition (1.87×10^{19} atoms/m²), M_{Ag} is the Ag molar mass, N_A is Avogadro's number, ρ_{Ag} is the bulk Ag density, and n is the Ag particle number density. The factor $f_{shadowing}$ is a shadowing factor which represents the additional interfacial area masked by the three-dimensional shape of the hemispherical particles at the incident and detection angles used.⁶⁸ For the analysis geometry used in these experiments (incident ions normal to the surface and detected ions measured at 45° from the surface normal), the shadowing factor is calculated to equal 1.207.⁶⁸ Since both θ and $[I(\theta)/I(\theta = \infty)]$ are measured, the only unknown variable in the above is the particle density n , which we determine by the best fit of equation (1) to the experimental data.

As shown in Figure 2, the best fits of this model to a series of multiple experiments at each temperature give particle densities of 4.4×10^{15} particles/m² at 300 K and 1.1×10^{16} particles/m² at 100 K. The particle density at 100 K is roughly 2.5 times larger than the particle density at 300 K. This is most likely due to the smaller diffusion constant of Ag adatoms across the surface at lower temperatures. Venable's theory of vapor deposited crystal growth predicts that the saturation particle density varies as the cube root of adatom diffusion constant (k_{diff}) for the same flux.⁶⁹ Applying that model to this data, we find that $k_{diff}(300 \text{ K})/k_{diff}(100 \text{ K}) \approx 2.5^3 \approx 16$, which implies an activation barrier for diffusion of $E_{diff} = R \ln(16) / [(1/100) - (1/300)] = 3.5$ kJ/mol. Density functional theory (DFT) calculations of the diffusion barrier for Ag / C(0001) from the literature report a diffusion barrier between 0.3 and 7.6 kJ/mol.^{24,50,70} The value for E_{diff} reported here falls within this range.

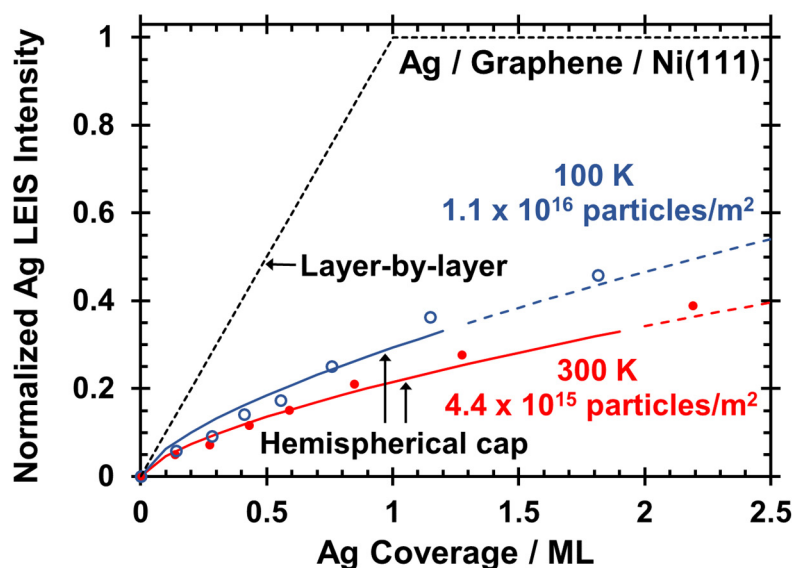


Figure 2: Integrated Ag LEIS signal normalized to a thick multilayer Ag film as a function of the Ag coverage after deposition onto graphene / Ni(111) at 300 K (red, filled points) and 100 K (blue, open points). The black dashed line corresponds to the LEIS signal that would be observed for a layer-by-layer growth mode for Ag atoms packing with the same areal density as Ni(111). The solid lines correspond to the Ag growing as hemispherical particles with a particle density of 4.4×10^{15} particles/m² at 300 K (red) and 1.1×10^{16} particles/m² at 100 K (blue). The dotted lines above the Ag coverages that give a normalized Ag LEIS signal of 0.33 are only a guide to the eye since the model should not be applied at those higher coverages.

Most experimental studies of evaporated films of Ag (either from Ag monomers or from small, mass-selected Ag cluster ions) on graphite(0001) or graphene surfaces found that the Ag agglomerates into 3D clusters at room temperature, as we find here.^{24,38–40,46} One early STM study reports “flat” Ag clusters referred to as 2D clusters on graphite, but that study was performed at very low coverages (~ 0.001 ML),⁴⁵ much lower than here.

3.4 Differential Heat of Adsorption of Ag on Graphene / Ni(111)

The differential heats of adsorption as a function of coverage of Ag onto graphene / Ni(111) at 300 K and 100 K are shown in Figure 3. Each point corresponds to a pulse of Ag vapor from the molecular beam (with ~ 0.012 ML per pulse) but averages several runs. The heats of adsorption here are corrected to account for the difference in internal energy between a flux of gas phase Ag atoms coming from a high temperature electron beam evaporator (~ 1380 K)⁵⁷ and a collection of the same gas atoms in a Boltzmann distribution at the surface temperature (300 K or 100 K), as described in previous work.⁶¹ In this way, the heat of adsorption equals the negative of the standard enthalpy of adsorption at that each temperature. At 300 K, the heat of adsorption initially starts at 230 kJ/mol and rapidly increases to 270 kJ/mol within the first 0.1 ML of deposition. The heats of adsorption then slowly increase until reaching a plateau of 280 kJ/mol

by 2 ML, which is within 1.8% of the reported enthalpy of sublimation of bulk Ag ($\Delta H_{\text{sub}} = 285$ kJ/mol).⁷¹

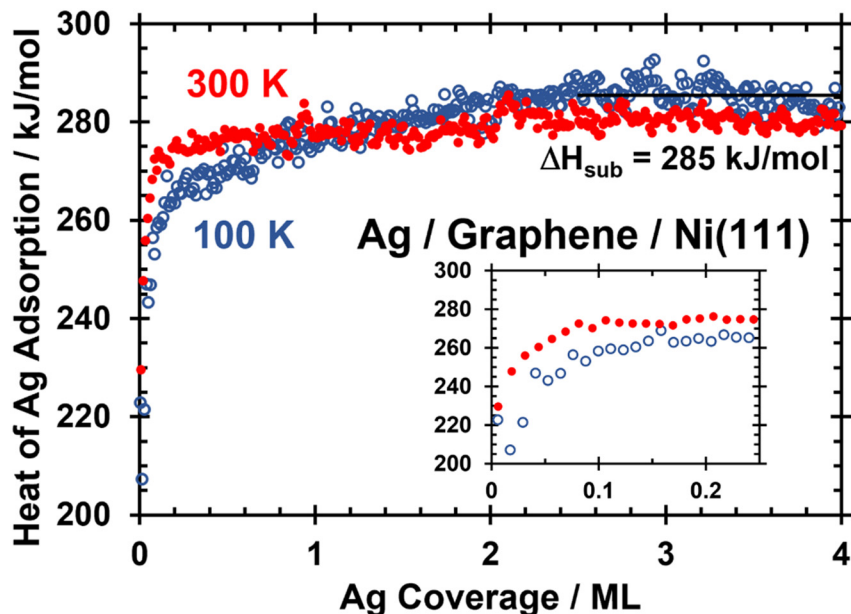


Figure 3: Differential heat of adsorption of Ag atoms onto graphene / Ni(111) as a function of Ag coverage at 300 K (red, filled points) and 100 K (blue, open points). The inset shows the low coverage regime (until 0.25 ML) on an expanded scale.

Due to errors (~10%) known to be present in calibrating the calorimeter’s absolute heat sensitivity factor for these graphene/Ni(111) surfaces, we adjusted this factor to ensure that the heat of adsorption and corresponding Ag chemical potential for the largest particle sizes measured (6-8 nm at 300 K, and 3-5 nm at 100 K) agreed with the model described below for chemical potential versus particle size (taken from references^{9,10}). This resulted in heats of adsorption at the highest coverages measured (3.5 to 4 ML) agreeing with the reported heat of sublimation of bulk solid Ag ($\Delta H_{\text{sub}} = 285$ kJ/mol) within 1.8% at 300 K and within 0.5% at 100 K.

At 100 K, the heat of adsorption of Ag onto graphene / Ni(111) is initially 223 kJ/mol and drops down to 207 kJ/mol by the second pulse of Ag gas. This initial decrease in the heat of adsorption, which was seen in every run at 100 K, might be due to the population of stronger-binding defect sites in the first gas pulse that get saturated by the second pulse. This effect might be washed out at 300 K by the more rapid growth in particle size at 300 K, where 2.5 times as many Ag atoms add to each cluster between the first and second pulses compared to 100 K (since there are 2.5 times fewer Ag clusters at 100 K). As shown below, the heat increases rapidly with particle size due to the formation of more Ag-Ag bonds to the newly arrived Ag atom when attaching to a larger Ag cluster. (For example, a Ag atom adding to a Ag_3 cluster can make three new Ag-Ag bonds at most, whereas it makes six Ag-Ag bonds (on average) when adding to Ag particles in the large-size limit.) After the initial decrease, the heat of adsorption at 100 K quickly rises to

reach ~ 275 kJ/mol by 0.5 ML and further increases slowly until the enthalpy of sublimation for bulk Ag is reached by 2.5 ML. The slower increase in the heats of adsorption with Ag coverage at 100 K than 300 K can again be explained by the fact that the particles are 2.5 times smaller at 100 K at any given coverage, so fewer Ag-Ag bonds are made when a new Ag atom is adsorbed at 100 K.

To better compare heats of adsorption with the same nanoparticle size between 300 K and 100 K, we show the heats of adsorption of Ag onto graphene / Ni(111) as a function of the effective particle diameter in Figure 4. The average effective particle diameter at any coverage is calculated from the total Ag coverage (in atoms per unit area) divided by the Ag particle density, which equals the average particle size in atom number. By assuming all particles have the density of bulk Ag(solid), this also gives the particle volume, which for the assumed hemispherical shape also provides the effective diameter. Besides the very small particle regime ($D_{\text{eff}} < 2$ nm), we observe a remarkable agreement in the heats as a function of particle size regardless of temperature. Except for this very small size regime, the heat of adsorption at both temperatures gradually increases with effective particle diameter. This is caused by the higher number of Ag-Ag bonds that can be formed by addition of a gas phase Ag atom to a larger particle. As the particles reach a bulk-like size (around 5 nm), the addition of another gas phase Ag atom comes very close to the bulk enthalpy of sublimation.

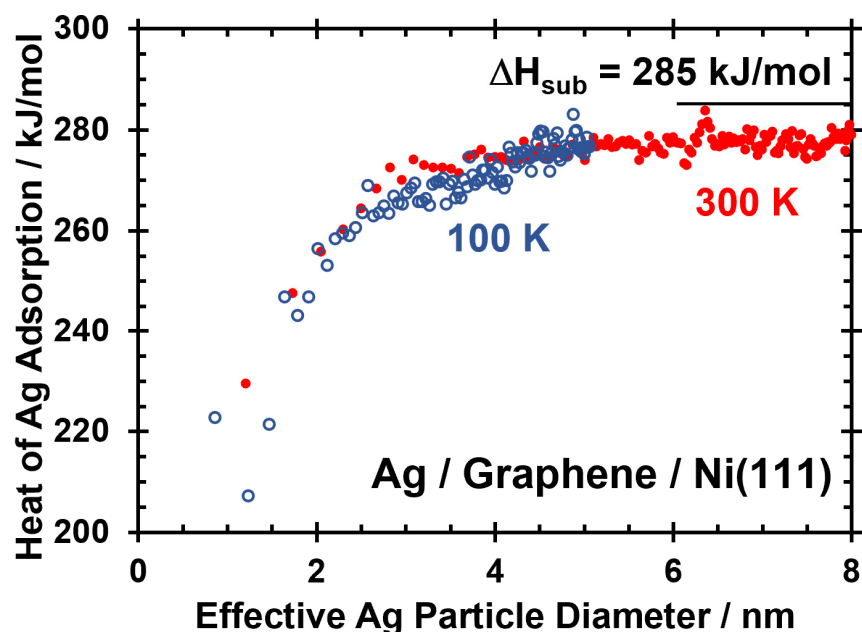


Figure 4: Differential heat of Ag adsorption on graphene / Ni(111) at 300 K (red, filled points) and 100 K (blue, open points) as a function of the effective Ag particle diameter to which Ag atoms add during particle growth.

The heats of adsorption in Figure 4 can be compared to DFT calculations of Ag monomers and clusters on graphite(0001) and graphene surfaces. Calculations of Ag monomer adsorption on

C(0001) show a very weak interaction (between about 0 and 76 kJ/mol) between Ag and C(0001),^{24,47,48,50-52} which could explain the very low sticking probability we observe, and is consistent with the low heats we observe for the smallest clusters (see below). One of these studies also included calculations of Ag monomer adsorption on a stepped graphite surface and showed a 15-30 kJ/mol preference for adsorption energy near the step-edge defect.⁴⁸ This is consistent with the 16 kJ/mol difference we measured between the first and second pulses of Ag deposition at 100 K, which we attributed to defect sites.

We can make a more direct comparison of our results with calculations which provide the energy change of gas phase Ag to form larger Ag clusters supported on C(0001).⁴⁹⁻⁵¹ These calculations all show that as the particles grow in size, the adsorption energy rapidly grows in magnitude as the Ag cohesive energy starts to dominate the monomer adsorption energy. One such study reports an energy change of -159 to -164 kJ per mole of Ag atoms for $13 \times \text{Ag}(\text{gas}) \rightarrow \text{Ag}_{13}(\text{adsorbed})$ for 3D Ag clusters on free-standing graphene.⁵¹ Another study found an energy change of -224 to -229 kJ per mole of Ag atoms for $n \times \text{Ag}(\text{gas}) \rightarrow \text{Ag}_n(\text{adsorbed})$ with $n = 7-9$ for pseudo epitaxial growth of 2D Ag on graphene / SiC(0001) (up from only -35 and -111 kJ/mol at $n = 1$ and 2, respectively).⁵⁰ These can be compared with the measured heat of adsorption in the first pulses of our experiments where the first pulse at 300 K forms clusters of ~26 atoms (on average) and an average heat of adsorption of 230 kJ/mol, and the first two pulses at 100 K form clusters of ~9 and ~30 atoms, respectively, with heats of adsorption of 223 kJ/mol and 207 kJ/mol, respectively. The differences between our experimental results and those calculations could be attributed to any of the following reasons: (1) the larger cohesive energy for the larger particles we studied, (2) stabilization of particles in our experiments by defect sites in the first pulse at 100 K, (3) stabilization of particles in our experiments due to long-range attractive interactions with the underlying Ni(111) substrate, (4) intrinsic errors in their DFT calculations or our experiments. While the exact details of these differences are unknown, it is promising that there is only a relatively small difference between those calculations and our experimental results despite the complicated system studied and slightly different substrates.

A recent study reported the heat of Ag vapor adsorption versus coverage on graphite measured using equilibrium adsorption isosteres at very high temperatures,⁷² but that approach seems unreasonable given the strong thermodynamic driving force for Ag on graphene to agglomerate into large particles as shown in Figures 4 and 5 above. Indeed, the Ag particles in that study were found to have diameters of a few hundred nanometers, and the sample had a lot of alumina particulate impurity.

3.5 Chemical Potential and Adhesion Energy of Ag Particles on Graphene / Ni(111)

If we neglect entropic contributions to the free energy (which are much smaller than enthalpic effects for supported metal nanoparticles), we can calculate the chemical potential of Ag atoms in supported metal nanoparticles. The chemical potential of metal atoms in supported nanoparticles relative to the bulk metal (set as a reference with zero chemical potential) is equal to the metal bulk heat of sublimation minus the differential heat of adsorption.¹¹ The resulting

chemical potential of Ag nanoparticles supported on graphene / Ni(111) as a function of the effective diameter is shown in Figure 5.

As seen in Figure 5, the Ag chemical potential rapidly decreases as the particle size increases, as has been shown for many metals supported on single crystal oxides.⁹ Previous work from our group has shown that the chemical potential of late transition metals supported on oxides as a function of diameter (D) is very well-approximated by:⁹

$$\mu(D) = (3\gamma_{v/M} - E_{adh})(1 + D_0/D)(2V_m/D) , \quad (2)$$

where $\gamma_{v/M}$ is the surface free energy of the bulk metal (1.22 J/m² for Ag),⁷³ E_{adh} is the adhesion energy of the metal / support interface (here the adhesion energy between bulk Ag and graphene / Ni(111)), V_m is the molar volume of the bulk metal (10.3 cm³/mol for Ag), and $(1 + D_0/D)$, with $D_0 = 1.5$ nm, is an empirical factor that has been shown to account for the increase in γ_M and E_{adh} (relative to their bulk values) as the supported particles decrease in size.⁹ If we keep $D_0 = 1.5$ as the empirical factor here, the only unknown remaining in eq (2) is E_{adh} .

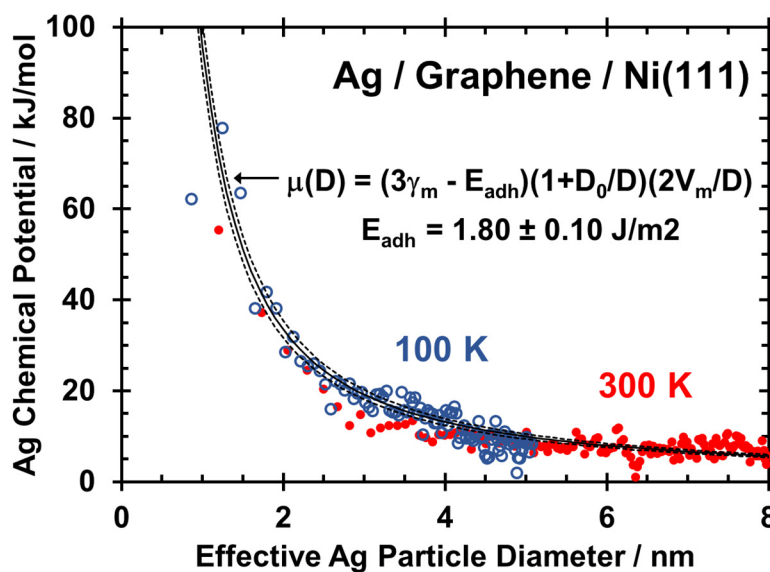


Figure 5: Chemical potential of Ag atoms in nanoparticles on graphene / Ni(111) vs the effective particle diameter at 300 K (red, filled points) and 100 K (blue, open points). The black solid line shows the hemispherical cap approximation (eq (2)) with $E_{adh} = 1.80$ J/m². The dotted black curve slightly above the solid black curve shows the same model (eq (2)) but with the value for E_{adh} determined by the integral-heat method ($E_{adh} = 1.70$ J/m²). The dotted black curve slightly below the solid black curve shows the best fit of that same hemispherical cap model (eq (2)) to the measured chemical potential versus size (combining both the 100 K and 300 K data, but omitting the first point at 100 K, which is attributed to defect sites). This fitting method gave the best-fit with the adjustable parameter $E_{adh} = 1.90$ J/m².

As discussed in previous work,^{10,74} the adhesion energy can be extracted from our calorimetric heat measurements in two main ways. The first method (described in detail in previous work from our group)^{1,75} is to use a conceptual three-step thermodynamic cycle that connects the heat of adsorption with the adhesion energy of a supported hemisphere (for the largest size measured). In the first step, the gaseous metal atoms form a free-standing hemispherical particle in vacuum. The energy change of this step is the negative sublimation enthalpy times the number of metal atoms ($-n \Delta H_{sub}$) plus the energy cost to form the hemispherical metal surface in vacuum ($+A [(1 + f) \gamma_{v/m}]$). Here A is the interfacial area between the metal particle and the support and $(1 + f)$ is a factor that accounts for the additional top surface area of the particle ($f = 2$ for hemispherical caps). In the second step, the metal hemisphere in vacuum is attached to the support surface with a downhill energy change of the interfacial area times the adhesion energy ($-A E_{adh}$). The overall energy change of these two steps is equal to the formation energy of the supported metal particles (from gas atoms), which can alternatively be expressed as the negative differential enthalpy of adsorption (or negative differential heat of adsorption measured calorimetrically), integrated from zero coverage up to the coverage that gives the largest effective particle diameter measured ($\sum \Delta H_{ads}$). Combining all steps of this cycle, the following equation results:^{1,75}

$$\sum_n \Delta H_{ads} = -n \Delta H_{sub} + A [(1 + f) \gamma_{v/m} - E_{adh}] . \quad (3)$$

This equation assumes that the particles' diameter (D) has reached the large-size limit for both $\gamma_{v/m}$ and E_{adh} , which is not the case here. We extend that integral here only up to $D = 8$ nm at 300 K and $D = 5$ nm at 100 K, due to possible particle overlap at larger particles sizes. The empirical correction factor of $(1 + D_0/D)$ was used in eq(2) to correct γ_M and E_{adh} for small particles (relative to their bulk values). When applied to the largest particles considered here, it shows that γ_M and E_{adh} are still 19-30% larger than the true large-size limit, and thus require the use of this correction factor to accurately calculate the adhesion energy. To account for the size dependence of surface energy and adhesion energies, we therefore introduce the same empirical correction factor of $(1 + D_0/D)$ used in eq (2) to slightly correct eq (3) as well, as was done previously.^{10,74} The resulting corrected equation is:

$$\sum_n \Delta H_{ads} = -n \Delta H_{sub} + A [(1 + f) \gamma_{v/m} - E_{adh}] \left(1 + \frac{D_0}{D}\right) , \quad (4)$$

where D is the largest effective diameter reached in the integrated heat term. The only parameter in eq (4) not provided in the literature or measured in our experiments is then the adhesion energy. Substituting the known values into eq (4) and solving, we calculate an adhesion energy of 1.72 J/m^2 using the heat data from 300 K, or 1.67 J/m^2 using the heat data from 100 K, with an average of 1.70 J/m^2 . The chemical potential fit of eq (2) using $E_{adh} = 1.70 \text{ J/m}^2$ overlaid on the measured chemical potential is shown in Figure 5 as a dotted black curve slightly above the solid black curve.

As mentioned above, the only unknown variable remaining in eq (2) is the adhesion energy. It follows that an alternative method to extract the adhesion energy from our calorimetric heat

measurements is to fit eq (2) to the measured Ag chemical potential. Since the lowest diameter chemical potential at 100 K is significantly stabilized by defects, we omit that point in the fitting process. Using all 300 K and 100 K chemical potential data except that lowest diameter point at 100 K, we find the best fit to eq (2) is with an adhesion energy of 1.90 J/m^2 . The fit of eq (2) with $E_{adh} = 1.90 \text{ J/m}^2$ is shown in Figure 5 as a dotted black curve slightly below the solid black curve. Without a clear reason to expect one of these methods is more accurate than the other, we assume the true adhesion energy of Ag to graphene / Ni(111) is given by the average of these two values with an uncertainty of $\sim 0.1 \text{ J/m}^2$. Thus, the adhesion energy of Ag particles supported on graphene / Ni(111) measured in these experiments is $E_{adh} = 1.80 \pm 0.10 \text{ J/m}^2$.

3.6 Comparison to Ag on Oxide Support Materials

This adhesion energy for Ag to graphene of $\sim 1.8 \text{ J/m}^2$ can be compared to those reported for Ag to MgO(100), CeO₂(111) and TiO₂(100) of 0.30 and 2.3 and 2.44 J/m^2 , respectively,^{13,74,76} showing that graphene on Ni binds Ag nanoparticles within the range measured on these oxides. It binds Ag almost as strongly as the most strongly-bonding of these oxide supports (CeO₂(111)), and much more strongly than the weakest (MgO(100)). As seen from eq (2), this means that for a given Ag nanoparticle size (below 6 nm) on these different supports, the Ag chemical potential will be considerably lower for Ag on this model carbon support compared to Ag on MgO(100), and slightly higher compared to Ag on CeO₂(111). This has two important implications with respect to catalyst performance. Given the quantitative kinetic relationship which shows that sintering rates for a given particle size increase with increasing chemical potential,^{9,13,14,16,77} this means that such a carbon support will be almost as effective as CeO₂ at reducing sintering rates and enhancing long-term catalyst sinter resistance to prevent deactivation, compare to weak-binding supports like MgO. Given the qualitative correlations which show that metal nanoparticles which possess lower metal chemical potential bond small adsorbed catalytic reaction intermediates (like O, OH, CH₃ and CO) more weakly,^{9-11,15} this means that, for a given Ag nanoparticle size, it will bind such small adsorbates more weakly when supported on such a carbon support than when supported on a weak-binding support like MgO, but slightly more strongly than when the support is CeO₂.

Recent theoretical estimates of adhesion energies for other oxides based on DFT^{78,79} may be useful in comparing these experimental adhesion energies of Ag to graphene and a few oxides (and their implications with respect to Ag chemical potential) to those from a broader range of oxides.

The sticking probability for Ag on graphene / Ni(111) (Fig. 1) is lower than was measured for Ag on any of these oxide surfaces.^{13,57,74,76} The value of 0.75 at 300 K is much lower than the smallest of those, 0.943 for Ag on MgO(100),⁷⁶ meaning that a Ag gas atom which strikes graphene is 4.4 times more likely to desorb again into the gas phase than when it hits MgO(100). Lower sticking probabilities are thought to correlate with weaker bonding of the metal monomer to the surface.⁸⁰ This weaker bonding also correlates with lower saturation number density of metal clusters, due to the kinetics of nucleation.⁸⁰ Indeed, this density seen here at 300 K ($4.4 \times 10^{15} / \text{m}^2$, Fig. 2) is ~ 6 -fold lower than for Ag on MgO(100).⁸⁰ It is clear that Ag monomers bond

significantly more weakly to graphene support than to any of the oxide supports that have been studied. This also has an important implication with respect to catalyst performance, specifically sinter resistance. The weaker the monomer bonds to the support surface, the slower is the rate of metal nanoparticle sintering (at the same temperature) for nanoparticles on different supports with the same metal chemical potential and number density.^{13,14,77}

4. Conclusions

The He⁺ LEIS growth mode experiments showed that Ag supported on graphene / Ni(111) grows with a particle number density of 4.4×10^{15} particles/m² at 300 K and 1.1×10^{16} particles/m² at 100 K. This difference is attributed to the higher mobility of Ag adatoms at 300 K with an estimated activation barrier for diffusion of ~3.5 kJ/mol. QMS measurements showed an initial sticking probability of 75% at 300 K and 85% at 100K. This is consistent with expectation, since the ratio of the desorption rate to the diffusion rate is much lower at 100 K than 300 K (since the activation energy for desorption is larger than for diffusion). The heat of Ag adsorption at 300 K is 230 kJ/mol initially but quickly rises to 270 kJ/mol in the first 0.1 ML of coverage and further increases to within 5 kJ/mol of the bulk Ag sublimation enthalpy (285 kJ/mol) by 2 ML. The increase in heat with coverage is due to the larger Ag nanoparticles at higher coverage, which bind Ag atoms more strongly. At 100 K, the heat of adsorption is 223 kJ/mol in the first metal pulse, but drops to 207 kJ/mol in the next pulse. The higher heats in the first Ag pulse at 100 K is attributed to the very small Ag clusters binding initially to stronger-binding defect sites on the graphene / Ni(111) surface, which saturate before the second pulse. Thereafter, the heat rises with coverage to nearly the bulk Ag sublimation enthalpy by 2 ML, again due to increasing Ag particle size as at 100 K. The Ag chemical potential determined from these heats of adsorption decreases as a function of nanoparticle size, shows a remarkable agreement between the two temperatures studied, and is well-approximated by eq (2). This is the same relationship developed by our group that describes the chemical potential of metals supported on oxide supports. The adhesion energy of Ag to graphene / Ni(111) determined from these heat measurements is 1.70 J/m² when calculated from the integral heat of adsorption at high coverage and is 1.90 J/m² when calculated by fitting the measured chemical potential to Eq. (2), giving an average of 1.80 ± 0.10 J/m². This adhesion energy, when compared to that for Ag on various oxide supports, and combined with eq (2) for then comparing the Ag chemical potential for nanoparticles of the same size on different supports, has important implications with respect to the performance of Ag catalysts on such carbon supports, as summarized just above.

Acknowledgements

The authors acknowledge the Department of Energy, Office of Basic Energy Sciences, under Grant Number DE-FG02-96ER14630, for support of this work.

References

- (1) Campbell, C. T. Ultrathin Metal Films and Particles on Oxide Surfaces: Structural, Electronic and Chemisorptive Properties. *Surf. Sci. Rep.* **1997**, *27*, 1–111.
- (2) Goodman, D. W. Model Studies in Catalysis Using Surface Science Probes. *Chem. Rev.* **1995**, *95*, 523–536.
- (3) Roling, L. T.; Li, L.; Abild-Pedersen, F. Configurational Energies of Nanoparticles Based on Metal-Metal Coordination. *J. Phys. Chem. C* **2017**, *121*, 23002–23010.
- (4) Valden, M.; Lai, X.; Goodman, D. W. Onset of Catalytic Activity of Gold Clusters on Titania with the Appearance of Nonmetallic Properties. *Science* **1998**, *281*, 1647–1650.
- (5) Cortright, R. D.; Dumesic, J. A. Kinetics of Heterogeneous Catalytic Reactions: Analysis of Reaction Schemes. *Adv. Catal.* **2001**, *46*, 161–264.
- (6) Tsunoyama, H.; Sakurai, H.; Negishi, Y.; Tsukuda, T. Size-Specific Catalytic Activity of Polymer-Stabilized Gold Nanoclusters for Aerobic Alcohol Oxidation in Water. *J. Am. Chem. Soc.* **2005**, *127*, 9374–9375.
- (7) Schubert, M. M.; Hackenberg, S.; Van Veen, A. C.; Muhler, M.; Plzak, V.; Behm, J. J. CO Oxidation over Supported Gold Catalysts -"Inert" and "Active" Support Materials and Their Role for the Oxygen Supply during Reaction. *J. Catal.* **2001**, *197*, 113–122.
- (8) Andersson, M. P.; Abild-Pedersen, F.; Remediakis, I. N.; Bligaard, T.; Jones, G.; Engbæk, J.; Lytken, O.; Horch, S.; Nielsen, J. H.; Sehested, J.; Rostrup-Nielsen, J. R.; Nørskov, J. K.; Chorkendorff, I. Structure Sensitivity of the Methanation Reaction: H₂-Induced CO Dissociation on Nickel Surfaces. *J. Catal.* **2008**, *255*, 6–19.
- (9) Campbell, C. T.; Mao, Z. Chemical Potential of Metal Atoms in Supported Nanoparticles: Dependence upon Particle Size and Support. *ACS Catal.* **2017**, *7*, 8460-8466. See also erratum: DOI: 10.1021/acscatal.
- (10) Mao, Z.; Campbell, C. T. Predicting a Key Catalyst-Performance Descriptor for Supported Metal Nanoparticles: Metal Chemical Potential. *ACS Catal.* **2021**, *11*, 8284-8291. See also erratum: DOI: 10.1021/acscatal.
- (11) Campbell, C. T.; Sellers, J. R. V. Anchored Metal Nanoparticles: Effects of Support and Size on Their Energy, Sintering Resistance and Reactivity. *Faraday Discussions.* 2013, pp 9–30.
- (12) Lahiri, J.; Miller, T. S.; Ross, A. J.; Adamska, L.; Oleynik, I. I.; Batzill, M. Graphene Growth and Stability at Nickel Surfaces. *New J. Phys.* **2011**, *13*, 025001.
- (13) Farmer, J. A.; Campbell, C. T. Ceria Maintains Smaller Metal Catalyst Particles by Strong Metal-Support Bonding. *Science* **2010**, *329*, 933–936.
- (14) Parker, S. C.; Campbell, C. T. Kinetic Model for Sintering of Supported Metal Particles with Improved Size-Dependent Energetics and Applications to Au on TiO₂ (110). *Phys. Rev. B - Condens. Matter Mater. Phys.* **2007**, *75*.
- (15) Campbell, C. T. The Energetics of Supported Metal Nanoparticles: Relationships to Sintering Rates and Catalytic Activity. *Acc. Chem. Res.* **2013**, *46*, 1712–1719.
- (16) Plessow, P. N.; Campbell, C. T. Influence of Adhesion on the Chemical Potential of Supported Nanoparticles as Modeled with Spherical Caps. *ACS Catal.* **2021**, Advance online publication. DOI: 10.1021/acscatal.
- (17) Singh, N.; Nguyen, M. T.; Cantu, D. C.; Mehdi, B. L.; Browning, N. D.; Fulton, J. L.; Zheng, J.; Balasubramanian, M.; Gutiérrez, O. Y.; Glezakou, V. A.; Rousseau, R.; Govind, N.; Camaioni, D. M.; Campbell, C. T.; Lercher, J. A. Carbon-Supported Pt during Aqueous Phenol Hydrogenation with and without Applied Electrical Potential: X-Ray

- Absorption and Theoretical Studies of Structure and Adsorbates. *J. Catal.* **2018**, *368*, 8–19.
- (18) Kim, C.; Jeon, H. S.; Eom, T.; Jee, M. S.; Kim, H.; Friend, C. M.; Min, B. K.; Hwang, Y. J. Achieving Selective and Efficient Electrocatalytic Activity for CO₂ Reduction Using Immobilized Silver Nanoparticles. *J. Am. Chem. Soc.* **2015**, *137*, 13844–13850.
 - (19) Song, Y.; Sanyal, U.; Pangotra, D.; Holladay, J. D.; Camaioni, D. M.; Gutiérrez, O. Y.; Lercher, J. A. Hydrogenation of Benzaldehyde via Electrocatalysis and Thermal Catalysis on Carbon-Supported Metals. *J. Catal.* **2018**, *359*, 68–75.
 - (20) Dieckmann, G. R.; Langer, S. H. Comparisons of Ebonex® and Graphite Supports for Platinum and Nickel Electrocatalysts. *Electrochim. Acta* **1998**, *44*, 437–444.
 - (21) Toebes, M. L.; Van Dillen, J. A.; De Jong, K. P. Synthesis of Supported Palladium Catalysts. *J. Mol. Catal. A Chem.* **2001**, *173*, 75–98.
 - (22) Yoo, E. J.; Okata, T.; Akita, T.; Kohyama, M.; Nakamura, J.; Honma, I. Enhanced Electrocatalytic Activity of Pt Subnanoclusters on Graphene Nanosheet Surface. *Nano Lett.* **2009**, *9*, 2255–2259.
 - (23) Nartova, A. V.; Bukhtiyarov, A. V.; Kvon, R. I.; Makarov, E. M.; Prosvirin, I. P.; Bukhtiyarov, V. I. Atomic Scale Structural Defects in the Graphite Layer for Model Catalysis. *Surf. Sci.* **2018**, *677*, 90–92.
 - (24) Appy, D.; Lei, H.; Wang, C. Z.; Tringides, M. C.; Liu, D. J.; Evans, J. W.; Thiel, P. A. Transition Metals on the (0001) Surface of Graphite: Fundamental Aspects of Adsorption, Diffusion, and Morphology. *Progress in Surface Science*. Pergamon August 1, 2014, pp 219–238.
 - (25) Batzill, M. The Surface Science of Graphene: Metal Interfaces, CVD Synthesis, Nanoribbons, Chemical Modifications, and Defects. *Surface Science Reports*. 2012, pp 83–115.
 - (26) Gebhardt, J.; Koch, R. J.; Zhao, W.; Höfert, O.; Gotterbarm, K.; Mammadov, S.; Papp, C.; Görling, A.; Steinrück, H. P.; Seyller, T. Growth and Electronic Structure of Boron-Doped Graphene. *Phys. Rev. B - Condens. Matter Mater. Phys.* **2013**, *87*, 155437.
 - (27) Koch, R. J.; Weser, M.; Zhao, W.; Viñes, F.; Gotterbarm, K.; Kozlov, S. M.; Höfert, O.; Ostler, M.; Papp, C.; Gebhardt, J.; Steinrück, H. P.; Görling, A.; Seyller, T. Growth and Electronic Structure of Nitrogen-Doped Graphene on Ni(111). *Phys. Rev. B - Condens. Matter Mater. Phys.* **2012**, *86*, 075401.
 - (28) Bao, X.; Muhler, M.; Pettinger, B.; Schlögl, R.; Ertl, G. On the Nature of the Active State of Silver during Catalytic Oxidation of Methanol. *Catal. Letters* **1993**, *22*, 215–225.
 - (29) Qu, Z.; Cheng, M.; Huang, W.; Bao, X. Formation of Subsurface Oxygen Species and Its High Activity toward CO Oxidation over Silver Catalysts. *J. Catal.* **2005**, *229*, 446–458.
 - (30) Zhang, X.; Qu, Z.; Li, X.; Wen, M.; Quan, X.; Ma, D.; Wu, J. Studies of Silver Species for Low-Temperature CO Oxidation on Ag/SiO₂ Catalysts. *Sep. Purif. Technol.* **2010**, *72*, 395–400.
 - (31) van den Hoek, P. J.; Baerends, E. J.; van Santen, R. A. Ethylene Epoxidation on Ag(110): The Role of Subsurface Oxygen. *J. Phys. Chem.* **1989**, *93*, 6469–6475.
 - (32) Serafin, J. G.; Liu, A. C.; Seyedmonir, S. R. Surface Science and the Silver-Catalyzed Epoxidation of Ethylene: An Industrial Perspective. *J. Mol. Catal. A Chem.* **1998**, *131*, 157–168.
 - (33) Shivakumar, M. S.; Krishnamurthy, G.; Ravikumar, C. R.; Bhatt, A. S. Decoration of Silver Nanoparticles on Activated Graphite Substrate and Their Electrocatalytic Activity

- for Methanol Oxidation. *J. Sci. Adv. Mater. Devices* **2019**, *4*, 290–298.
- (34) Tan, C.; Wang, F.; Liu, J.; Zhao, Y.; Wang, J.; Zhang, L.; Park, K. C.; Endo, M. An Easy Route to Prepare Carbon Black-Silver Hybrid Catalysts for Electro-Catalytic Oxidation of Hydrazine. *Mater. Lett.* **2009**, *63*, 969–971.
- (35) Zahed, B.; Hosseini-Monfared, H. A Comparative Study of Silver-Graphene Oxide Nanocomposites as a Recyclable Catalyst for the Aerobic Oxidation of Benzyl Alcohol: Support Effect. *Appl. Surf. Sci.* **2015**, *328*, 536–547.
- (36) Christopher, P.; Xin, H.; Linic, S. Visible-Light-Enhanced Catalytic Oxidation Reactions on Plasmonic Silver Nanostructures. *Nat. Chem.* **2011**, *3*, 467–472.
- (37) Gao, S.; Zhang, Z.; Liu, K.; Dong, B. Direct Evidence of Plasmonic Enhancement on Catalytic Reduction of 4-Nitrophenol over Silver Nanoparticles Supported on Flexible Fibrous Networks. *Appl. Catal. B Environ.* **2016**, *188*, 245–252.
- (38) Zhou, H.; Qiu, C.; Yu, F.; Yang, H.; Chen, M.; Hu, L.; Sun, L. Thickness-Dependent Morphologies and Surface-Enhanced Raman Scattering of Ag Deposited on n-Layer Graphenes. *J. Phys. Chem. C* **2011**, *115*, 11348–11354.
- (39) Huang, C. wen; Lin, H. Y.; Huang, C. H.; Shiue, R. J.; Wang, W. H.; Liu, C. Y.; Chui, H. C. Layer-Dependent Morphologies of Silver on n-Layer Graphene. *Nanoscale Res. Lett.* **2012**, *7*, 1–6.
- (40) Goldby, I. M.; Kuipers, L.; Von Issendorff, B.; Palmer, R. E. Diffusion and Aggregation of Size-Selected Silver Clusters on a Graphite Surface. *Appl. Phys. Lett.* **1996**, *69*, 2819–2821.
- (41) Francis, G. M.; Goldby, I. M.; Kuipers, L.; Von Issendorff, B.; Palmer, R. E. Deposition and Growth of Noble Metal Clusters on Graphite. *J. Chem. Soc. - Dalt. Trans.* **1996**, No. 5, 665–671.
- (42) Jackson, J. G.; Fonesca, R. W.; Holcombe, J. A. Detection of Surface Aggregates of Trace Amounts of Copper and Silver on Graphite Using Secondary Ion Mass Spectrometry at Elevated Temperatures. *J. Anal. At. Spectrom.* **1994**, *9*, 167–170.
- (43) Schaffner, M. H.; Jeanneret, J. F.; Patthey, F.; Schneider, W. D. An Ultrahigh Vacuum Sputter Source for in Situ Deposition of Size-Selected Clusters: Ag on Graphite. *J. Phys. D. Appl. Phys.* **1998**, *31*, 3177–3184.
- (44) Ganz, E.; Sattler, K.; Clarke, J. Scanning Tunneling Microscopy of Silver, Gold, and Aluminum Monomers and Small Clusters on Graphite. *J. Vac. Sci. Technol. A Vacuum, Surfaces, Film.* **1988**, *6*, 419–423.
- (45) Ganz, E.; Sattler, K.; Clarke, J. Scanning Tunneling Microscopy of the Local Atomic Structure of Two-Dimensional Gold and Silver Islands on Graphite. *Phys. Rev. Lett.* **1988**, *60*, 1856–1859.
- (46) Ndlovu, G. F.; Roos, W. D.; Wang, Z. M.; Asante, J. K. O.; Mashapa, M. G.; Jafta, C. J.; Mwakikunga, B. W.; Hillie, K. T. Epitaxial Deposition of Silver Ultra-Fine Nanoclusters on Defect-Free Surfaces of HOPG-Derived Few-Layer Graphene in a UHV Multi-Chamber by in Situ STM, Ex Situ XPS, and Ab Initio Calculations. *Nanoscale Res. Lett.* **2012**, *7*, 1–8.
- (47) Wang, G. M.; BelBruno, J. J.; Kenny, S. D.; Smith, R. Interaction of Silver Adatoms and Dimers with Graphite Surfaces. *Surf. Sci.* **2003**, *541*, 91–100.
- (48) Ambrusi, R. E.; García, S. G.; Pronsato, M. E. Formation of Ag Nanowires on Graphite Stepped Surfaces. A DFT Study. *Appl. Surf. Sci.* **2015**, *324*, 710–717.
- (49) Jadoon, T.; Carter-Fenk, K.; Siddique, M. B. A.; Herbert, J. M.; Hussain, R.; Iqbal, S.;

- Iqbal, J.; Ayub, K. Silver Clusters Tune up Electronic Properties of Graphene Nanoflakes: A Comprehensive Theoretical Study. *J. Mol. Liq.* **2020**, *297*, 111902.
- (50) Shteplyuk, I.; Yakimova, R. Computational Appraisal of Silver Nanocluster Evolution on Epitaxial Graphene: Implications for CO Sensing. *ACS Omega* **2021**, *6*, 24739–24751.
- (51) Jalkanen, J. P.; Halonen, M.; Fernández-Torre, D.; Laasonen, K.; Halonen, L. A Computational Study of the Adsorption of Small Ag and Au Nanoclusters on Graphite. *J. Phys. Chem. A* **2007**, *111*, 12317–12326.
- (52) Amft, M.; Lebègue, S.; Eriksson, O.; Skorodumova, N. V. Adsorption of Cu, Ag, and Au Atoms on Graphene Including van Der Waals Interactions. *J. Phys. Condens. Matter* **2011**, *23*, 395001.
- (53) Dahal, A.; Batzill, M. Graphene–Nickel Interfaces: A Review. *Nanoscale* **2014**, *6*, 2548–2562.
- (54) Zhao, W.; Kozlov, S. M.; Höfert, O.; Gotterbarm, K.; Lorenz, M. P. A.; Viñes, F.; Papp, C.; Görling, A.; Steinrück, H. P. Graphene on Ni(111): Coexistence of Different Surface Structures. *J. Phys. Chem. Lett.* **2011**, *2*, 759–764.
- (55) Winterlin, J.; Bocquet, M. L. Graphene on Metal Surfaces. *Surf. Sci.* **2009**, *603*, 1841–1852.
- (56) Sellers, J. R. V.; James, T. E.; Hemmingson, S. L.; Farmer, J. A.; Campbell, C. T. Adsorption Calorimetry during Metal Vapor Deposition on Single Crystal Surfaces: Increased Flux, Reduced Optical Radiation, and Real-Time Flux and Reflectivity Measurements. In *Review of Scientific Instruments*; 2013; Vol. 84, pp 123901–123901.
- (57) Farmer, J. A.; Baricuatro, J. H.; Campbell, C. T. Ag Adsorption on Reduced CeO₂(111) Thin Films. *J. Phys. Chem. C* **2010**, *114*, 17166–17172.
- (58) King, D. A.; Wells, M. G. Reaction Mechanism in Chemisorption Kinetics: Nitrogen on the {100} Plane of Tungsten. *Proc. R. Soc. London. A. Math. Phys. Sci.* **1974**, *339*, 245–269.
- (59) Goodman, D. W.; Kelley, R. D.; Madey, T. E.; Yates, J. T. Kinetics of the Hydrogenation of CO over a Single Crystal Nickel Catalyst. *J. Catal.* **1980**, *63*, 226–234.
- (60) Coad, J. P.; Rivière, J. C. Auger Spectroscopy of Carbon on Nickel. *Surf. Sci.* **1971**, *25*, 609–624.
- (61) Stuckless, J. T.; Frei, N. A.; Campbell, C. T. A Novel Single-Crystal Adsorption Calorimeter and Additions for Determining Metal Adsorption and Adhesion Energies. *Rev. Sci. Instrum.* **1998**, *69*, 2427–2438.
- (62) Hemmingson, S. L.; Feeley, G. M.; Miyake, N. J.; Campbell, C. T. Energetics of 2D and 3D Gold Nanoparticles on MgO(100): Influence of Particle Size and Defects on Gold Adsorption and Adhesion Energies. *ACS Catal.* **2017**, *7*, 2151–2163.
- (63) Mao, Z.; Zhao, W.; Al-Mualem, Z. A.; Campbell, C. T. Energetics and Structure of Nickel Atoms and Nanoparticles on MgO(100). *J. Phys. Chem. C* **2020**, *124*, 14685–14695.
- (64) Mikhailov, S. N.; van den Oetelaar, L. C. A.; Brongersma, H. H. Strong Matrix Effect in Low-Energy He⁺ Ion Scattering from Carbon. *Nucl. Inst. Methods Phys. Res. B* **1994**, *93*, 210–214.
- (65) van den Oetelaar, L. C. A.; Mikhailov, S. N.; Brongersma, H. H. Mechanism of Neutralization in Low-Energy He⁺ Ion Scattering from Carbide and Graphitic Carbon Species on Rhenium. *Nucl. Inst. Methods Phys. Res. B* **1994**, *85*, 420–423.
- (66) Luna, N. B.; Bonetto, F. J.; Vidal, R. A.; Goldberg, E. C.; Ferrón, J. Low Energy Ion Scattering in He/HOPG System. *J. Mol. Catal. A Chem.* **2008**, *281*, 237–240.

- (67) Diebold, U.; Pan, J. M.; Madey, T. E. Growth Mode of Ultrathin Copper Overlayers on TiO₂(110). *Phys. Rev. B* **1993**, *47*, 3868–3876.
- (68) Campbell, C. T.; James, T. E. Ion Scattering Spectroscopy Intensities for Supported Nanoparticles: The Hemispherical Cap Model. *Surf. Sci.* **2015**, *641*, 166–169.
- (69) Venables, J. A. Atomic Processes in Crystal Growth. *Surf. Sci.* **1994**, *299–300*, 798–817.
- (70) Liu, X.; Han, Y.; Evans, J. W.; Engstfeld, A. K.; Behm, R. J.; Tringides, M. C.; Hupalo, M.; Lin, H. Q.; Huang, L.; Ho, K. M.; Appy, D.; Thiel, P. A.; Wang, C. Z. Growth Morphology and Properties of Metals on Graphene. *Progress in Surface Science.* **2015**, *90*, 397–443.
- (71) Haynes, W. M., Ed., *CRC Handbook of Chemistry and Physics*, 95th ed.; CRC Press, Boca Raton, FL, 2014.
- (72) Walton, K. L.; Jacobson, N. S.; Kowalski, B. A.; Brockman, J. D.; Loyalka, S. K. Sorption Isotherms and Isotherms of Silver on NBG-17 Graphite. *J. Nucl. Mater.* **2021**, *557*, 153264.
- (73) Vitos, L.; Ruban, A. V.; Skriver, H. L.; Kollar, J. The Surface Energy of Metals. *Surf. Sci.* **1998**, *411*, 186–202.
- (74) Mao, Z.; Rumpitz, J. R.; Campbell, C. T. Energetics of Ag Adsorption on and Adhesion to Rutile TiO₂(100) Studied by Microcalorimetry. *J. Phys. Chem. C* **2021**, *125*, 3036–3046.
- (75) Stuckless, J. T.; Starr, D. E.; Bald, D. J.; Campbell, C. T. Metal Adsorption Calorimetry and Adhesion Energies on Clean Single-Crystal Surfaces. *J. Chem. Phys.* **1997**, *107*, 5547–5553.
- (76) Larsen, J. H.; Ranney, J. T.; Starr, D. E.; Musgrove, J. E.; Campbell, C. T. Adsorption Energetics of Ag on MgO(100). *Phys. Rev. B* **2001**, *63*, 195410.
- (77) Wynblatt, P.; Gjostein, N. A. Supported Metal Crystallites. *Progress in Solid State Chemistry*. Pergamon January 1, 1975, pp 21–58.
- (78) Dietze, E. M.; Plessow, P. N. Predicting the Strength of Metal-Support Interaction with Computational Descriptors for Adhesion Energies. *J. Phys. Chem. C* **2019**, *123*, 20443–20450.
- (79) Hu, S.; Li, W.-X. Sabatier Principle of Metal-Support Interaction for Design of Ultrastable Metal Nanocatalysts. *Science* **2021**, *374*, 1360–1365.
- (80) Campbell, C. T.; Starr, D. E. Metal Adsorption and Adhesion Energies on MgO(100). *J. Am. Chem. Soc.* **2002**, *124*, 9212–9218.

Table of Contents Image

